Acta Pharmaceutica Sinica B 2026;16(1):470−483

Chinese Pharmaceutical Association
Institute of Materia Medica, Chinese Academy of Medical Sciences

Acta Pharmaceutica Sinica B

www.elsevier.com/locate/apsb
www.sciencedirect.com

ORIGINAL ARTICLE

Construction of a localized immune niche *via* supramolecular hydrogel vaccine to elicit durable and enhanced immunity against infectious diseases

Qi Shang[a], Chenwei Jiang[a], Xiaolong Wang[b], Mingmei Guo[a], Jing Liu[b], Zhedong Jin[b], Yunsheng Yuan[b], Feihu Wang[a,*]

[a]*School of Biomedical Engineering, Shanghai Jiao Tong University, Shanghai 200240, China*
[b]*Engineering Research Center of Cell & Therapeutic Antibody, Ministry of Education, School of Pharmacy, Shanghai Jiao Tong University, Shanghai 200240, China*

Received 1 April 2025; received in revised form 23 August 2025; accepted 1 September 2025

KEY WORDS

Self-assembling peptide;
Supramolecular nanofiber;
Hydrogel scaffold;
Immune niche;
Vaccine;
Infectious disease;
Single vaccination;
Durable immunity

Abstract Vaccines represent one of the most potent strategies for protecting humans from the threat of infectious diseases. Conventional vaccines elicit acquired immunity by mimicking pathogen characteristics; however, their protective efficacy is limited by inadequate spatiotemporal control of antigen delivery, resulting in suboptimal antigen exposure in lymphoid tissues and transient adaptive immune activation. Here, we developed a self-assembling peptide-based supramolecular hydrogel vaccine to establish a localized immune niche, demonstrating its remarkable efficacy in inducing durable and potent immunity against infectious diseases. We found that this *in situ*-formed supramolecular hydrogel vaccine serves as a reservoir for antigens and adjuvants while recruiting antigen-presenting dendritic cells (DCs) to accumulate within the scaffold. With the aid of adjuvant, the DCs exhibit enhanced antigen processing and presentation, creating an immunologically active niche that triggers robust B cell and T cell responses. Following a single vaccination, mice immunized with the hydrogel vaccine developed robust humoral immunity and sustained antibody production for 112 days, achieving potent neutralization activity. This study offers a novel approach to spatiotemporal control of vaccine responses that enables durable and enhanced immunity against infectious diseases.

*Corresponding author.
E-mail address: fhwang21@sjtu.edu.cn (Feihu Wang).

Peer review under the responsibility of Chinese Pharmaceutical Association and Institute of Materia Medica, Chinese Academy of Medical Sciences.

https://doi.org/10.1016/j.apsb.2025.09.014

1. Introduction

Vaccines are a frontline strategy to prevent and control the transmission of infectious diseases by activating the body's adaptive immune system, aiming to establish a herd immunity[1-3]. Conventional vaccines, such as NVX-CoV2373, BBIBP-CorV, and mRNA-1273, have been approved to prevent coronavirus disease 2019 (COVID-19), a prevalent infectious disease caused by the severe acute respiratory syndrome coronavirus 2 (SARS-CoV-2)[4-7]. However, the immunogenic effectiveness of conventional vaccines is substantially constrained by suboptimal delivery systems, coupled with inherent susceptibility of these vaccines to enzymatic degradation and premature clearance by the mononuclear phagocyte system[8,9]. Although some vaccine components reach nearby lymph nodes through the draining lymphatic vessels, the process is limited by poor lymph node targeting and insufficient antigen enrichment, which compromises the efficiency of antigen uptake and processing by antigen-presenting DCs, resulting in transient and suboptimal immune response[10,11]. Clinically, repeated vaccinations and higher doses are employed to sustain long-term immunological protection; however, these approaches are constrained by complex administration processes, as well as challenges in vaccine transport and storage, limiting their widespread clinical application[12]. Therefore, strategies to enhance the efficient exposure of antigens to antigen-presenting DCs would significantly improve vaccine efficacy by eliciting robust and durable immune responses after a single dose.

Spatiotemporal control of vaccine response to enhance interactions between the vaccine components and antigen presenting DCs represents a promising strategy to overcome key challenges of conventional vaccines, such as rapid clearance and poor lymph node targeting during *in vivo* migration[13-17]. The establishment of an immune niche can serve as an alternative platform for direct interaction between vaccine components and DCs, thereby promoting immune cell activation and shaping subsequent immune responses[18,19]. In particular, scaffold-based biomaterials can be utilized to create immune niche microenvironments, where the interconnected scaffold network provides a space for immune cells to reside and interact[20-22]. Building on this premise, we propose that employing a scaffold to create a depot for antigens and adjuvants, while recruiting antigen-presenting DCs to concentrate within the scaffold, enables these DCs to efficiently internalize the abundant antigens concentrated within the reservoir. Facilitated by adjuvants, the DCs undergo enhanced antigen processing and presentation, establishing an immunologically active niche. Subsequently, mature DCs migrate to lymph nodes, engaging B and T cells and eliciting a potent adaptive immune response. Furthermore, prolonged retention of antigens and adjuvants at the target site, coupled with sustained interactions among immune cells, could elicit durable protective immunity following a single vaccination.

Notably, supramolecular hydrogel scaffolds engineered through peptide self-assembly have demonstrated excellent biosafety, biocompatibility, and multifunctionality. These scaffolds serve as effective drug depots, enhancing local drug retention and enabling controlled drug release, thereby improving drug bioavailability at the target site while reducing off-target toxicity[23-27]. The fabrication of supramolecular hydrogel scaffolds involves a solvent-driven self-assembly process, wherein peptide molecules form nanofiber frameworks that subsequently organize into three-dimensional networked structures through entanglement and folding[28-30]. We have recently shown that supramolecular hydrogels are well suited for the localized delivery of immune modulators, with payload release significantly prolonged through molecular or electrostatic interactions[31-33]. In particular, the rapid "solution-to-hydrogel" transition under physiological conditions allows for minimally invasive subcutaneous injection, improving vaccinee compliance[34-36]. Based on these findings, we hypothesized that a supramolecular hydrogel vaccine could establish an immune niche, enabling sustained release of antigens and adjuvants to activate DCs and elicit a durable, potent immune response.

Herein, we developed a self-assembling peptide-based supramolecular hydrogel vaccine to construct a localized immune niche, demonstrating its high potency in eliciting durable and enhanced immunity against infectious diseases (Fig. 1). The model antigen, the receptor binding domain (RBD), derived from SARS-CoV-2, along with the adjuvant CpG oligonucleotide (CpG ODN) and granulocyte-macrophage colony-stimulating factor (GM-CSF, to recruit DCs to the hydrogel scaffold), were condensed onto a nanofiber composed of the self-assembling peptide KFKFEFKFE (KKFE8). This assembly resulted in the formation of a supramolecular hydrogel vaccine *in situ*, termed RCG/K8F. This hydrogel created an immune niche that facilitated prolonged antigen exposure to DCs within its scaffold and induced robust B and T cell responses. Our findings indicated that RCG/K8F hydrogel vaccine generated persistent antibodies with a potent neutralizing activity and served as a universal vaccine platform by incorporating mutated RBD antigens to combat evolving SARS-CoV-2 variants.

2. Materials and methods

2.1. Materials

RBD was purchased from Novoprotein Scientific Inc. (Suzhou, China). CpG ODN and GM-CSF were provided by InvivoGen (Toulouse, France). Th1/Th2 Mouse Uncoated ELISA Kit, Quant-iT OliGreen ssDNA, and GM-CSF ELISA Kit were provided by ThermoFisher Scientific Inc. (MA, USA). PE anti-CD86, eFluor™450 anti-CD80, PE anti-CD8, APC anti-CD19, APC anti-CD3, FITC anti-CD11c, FITC anti-CD4, APC/Fire™750 anti-CD45, APC/Cyanine7 anti-CD45, FITC anti-CD11b, PerCP/Cyanine5.5 anti-CD19, APC anti-CD27, APC anti-CD62L, Brilliant Violet 421™ anti-CD44, APC/Cyanine7 anti-CD3, PE/Cyanine7 anti-CD4, FITC anti-CD8, APC anti-IL-17, Brilliant Violet 421™ anti-IL-4, and PE anti-IFN-γ antibodies were purchased from BioLegend (CA, USA). The phosphate buffered saline (PBS) and bovine albumin (BSA) were purchased from Meilun Biotech Co., Ltd. (Dalian, China). The goat anti-mouse IgG (H + L)-HRP, goat anti-mouse IgM-HRP, goat anti-mouse IgG1-HRP, and goat anti-mouse IgG2b-HRP were provided by

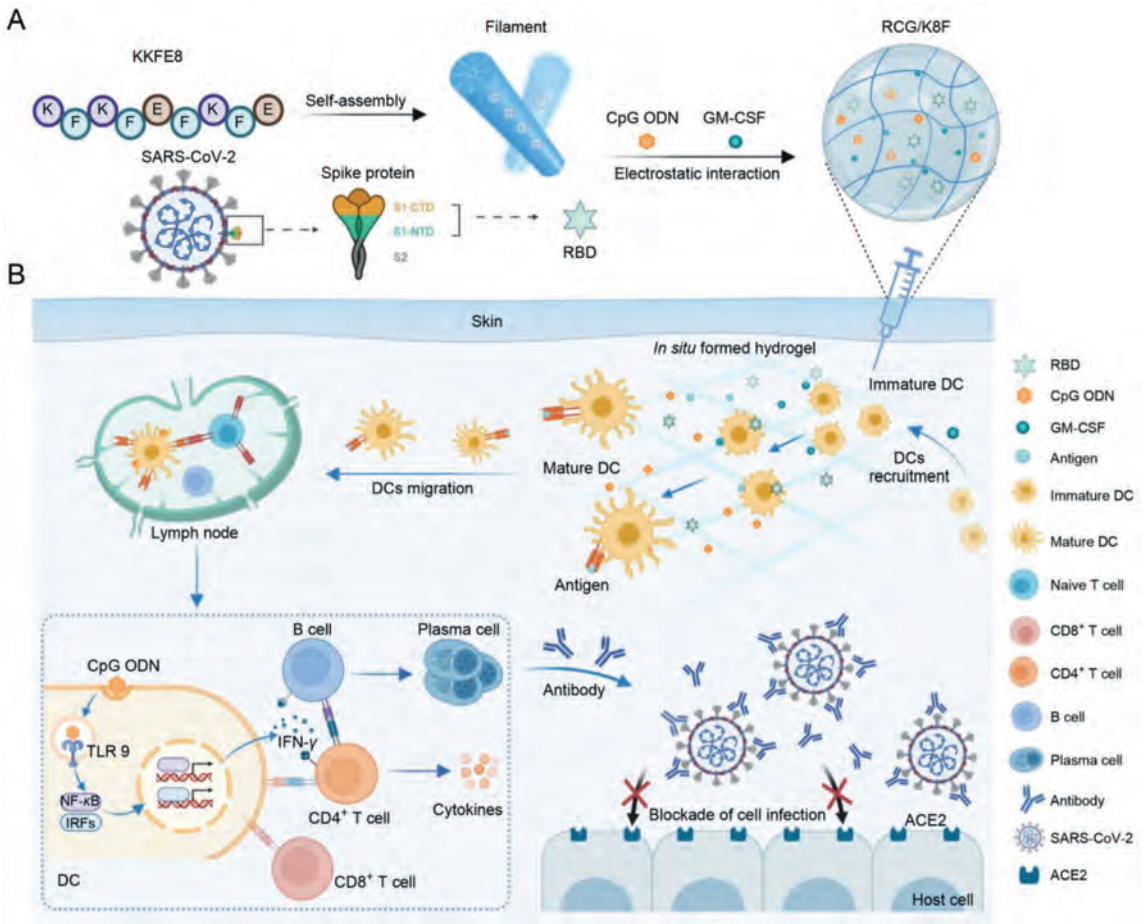

Figure 1 Schematic illustration of the RCG/K8F hydrogel vaccine creates an immune niche for spatiotemporal orchestration of adaptive immunity. (A) Schematic representation of the RCG/K8F fabrication process. (B) Schematic illustration of the immunomodulatory mechanism of RCG/K8F. After vaccination, this *in situ* formed RCG/K8F hydrogel vaccine locally recruits immature DCs to the hydrogel scaffold in response to GM-CSF. Within this scaffold, the immature DCs capture and process the antigen, facilitated by adjuvants, and transform into mature DCs. Subsequently, these antigen-loaded mature DCs migrate to the lymph node, activating both cellular and humoral immunity by inducing $CD8^+$ T-cell activation and antibody production, thereby conferring long-term protection against subsequent viral infection.

Southern Biotech (AL, USA). Mouse IFN-γ ELISpot Kit (ALP) was provided by MABTECH (Stockholm, Sweden).

2.2. *Preparation and identification of K8F*

The peptide KFKFEFKFE (KKFE8) was synthesized *via* solid-phase synthesis on a Liberty Lite automated microwave peptide synthesizer, followed by purification using preparative high-performance liquid chromatography (HPLC). The purified product was collected after freeze-drying. Matrix-assisted laser desorption ionization (MALDI) mass spectrometry (MS) was used to identity the molecular weight. KKFE8 was dissolved in deionized water and stored at room temperature for at least 24 h to facilitate self-assembly into filamentous structure (designated K8F). Transmission electron microscopy (Talos F200C G2) was performed to observe the particle size and morphology using negative staining with 2% phosphotungstic acid. Surface zeta potential was measured using a Zetasizer Nano.

The solution-hydrogel transition of K8F was evaluated by combining 180 μL of K8F solution with 20 μL of 10 × PBS in a clear glass vial, followed by assessment of hydrogel formation using the vial inversion method. The real-time gelation properties of K8F were further determined using a rheometer. 180 μL of the K8F solution was added into the rheometer tray to perform a time scan, and 20 μL of 10 × PBS was added to the solution using a syringe after 60 s. The gelation kinetics of K8F were evaluated by measuring the changes in storage modulus (G') and loss modulus (G'') over time.

2.3. *Preparation and characterization of RCG/K8F*

The vaccine components, including RBD (R, 10 μg), CpG ODN (C, 100 μg), and GM-CSF (G, 2 μg), were added to the K8F solution and incubated at 37 °C for 30 min to prepare the RCG/K8F; unbound components were removed by centrifugation and washing cycles. The zeta potential of the RCG/K8F solution was measured using a Zetasizer Nano instrument. The drug loading content was calculated according to Eq. (1):

$$\text{Drug loading content}\ (\%) = \frac{\text{Weight of loaded drug}}{\text{Weight of RCG/K8F}} \times 100 \qquad (1)$$

The RCG/K8F hydrogel was subsequently prepared by adding PBS to the RCG/K8F solution. Morphological characterization was performed using scanning electron microscope (SEM;

TESCAN VEGA 3). Prior to observation, hydrogel samples were flash-frozen in liquid nitrogen, lyophilized, and sputter-coated with a gold layer to ensure sufficient conductivity.

2.4. *In vitro drug release from RCG/K8F hydrogel*

180 μL of RCG/K8F solution (labeled RBD with Cy5, with excess Cy5 dye removed by dialysis) was placed in a 0.6 mL centrifuge tube, and 20 μL of 10 × PBS was added to induce the formation of the RCG/K8F hydrogel. Subsequently, 1 × PBS solution was added into the centrifuge tube as the release medium. At predetermined time points, the supernatant was collected and replaced with an equal volume of fresh 1 × PBS solution. The cumulative release of RBD, CpG ODN, and GM-CSF was measured by fluorescence intensity (for Cy5-RBD), the Quant-iT OliGreen ssDNA assay (for CpG ODN), and GM-CSF ELISA Kit, respectively, using a microplate reader.

2.5. *Animals*

6- to 8-week-old female BALB/c mice were purchased from SLAC Laboratory Animal Co., Ltd. (Shanghai, China). All animal experiments complied with the Health Guide for the Care and Use of Laboratory the Animals in National Institutes and the Ethics Review of Animal Experiment at Shanghai Jiao Tong University (Approval No. SYXK (Hu) 2018-0028, China).

2.6. *Biosafety evaluation of RCG/K8F in vivo*

To assess the systemic biosafety of RCG/K8F, blood samples and major organs (heart, liver, spleen, lung, and kidney) were collected and analyzed following 20 days of treatment. Blood samples were processed immediately after collection: one aliquot was transferred into EDTA-coated tubes for complete blood count analysis to evaluate potential hematopoietic effects; another aliquot was centrifuged to isolate serum for biochemical profiling. Major organs were harvested, fixed, and embedded for sectioning. Tissue sections were stained with hematoxylin and eosin (H&E) and examined under a light microscope to identify any histopathological changes indicative of treatment-related toxicity.

2.7. *In vivo gelation evaluation and drug biodistribution*

RCG/K8F (100 μL) was injected subcutaneously into 6- to 8-week-old female BALB/c mice. The gelation of the RCG/K8F was visibly confirmed and photographed 20 min after subcutaneous injection. To evaluate biodistribution and retention, Cy5-labeled RBD within RCG/K8F was injected subcutaneously into the BALB/c mice. The accumulation of RBD at the injection site and *in vivo* biodistribution were monitored *via* an IVIS spectrum imaging system (PerkinElmer, MA, USA) immediately and at 20 min, 3, 5, 10, and 15 days after vaccination. Fluorescence intensity was quantified to determine the release of RBD from Bolus and RCG/K8F hydrogel *in vivo*, respectively.

2.8. *Vaccine treatment protocol*

6- to 8-week-old female BALB/c mice were subcutaneously injected with 100 μL of normal saline (NS), K8F, Bolus (free RBD + CpG ODN + GM-CSF), RC/K8F, or RCG/K8F, as appropriate. The dosage of RBD, CpG ODN and GM-CSF is 10, 100 and 2 μg, respectively. Lymph nodes and spleens were collected to detect the immune cell infiltration and activation on Days 14 and 28, respectively. At predesignated time points, blood samples were acquired through the eye orbital vein and collected into a 1.5 mL EP tube by a capillary tube which was presoaked in 1% heparin, then stored at 4 °C fridge and afterward centrifuged at 860 × *g* for 15 min. The supernatant was collected on Days 14 and 28 for cytokine analysis. Blood samples were collected at 14-day intervals starting on Day 14 to measure anti-RBD antibody production.

2.9. *Cellular immune response analysis*

6- to 8-week-old female BALB/c mice were subcutaneously injected with NS, K8F, Bolus, RC/K8F, and RCG/K8F. The lymph node and the spleen were excised 14 days and 28 days after vaccination. After digestion and filtration, the cell resuspension was labeled with fluorescence-conjugated anti-mouse antibodies. Flow cytometry was used to detect the activation and infiltration of immune cells in the lymph node, hydrogel, and spleen. Cytokine secretion was quantified by Th1/Th2 Mouse Uncoated ELISA Kit. The mouse serum samples were diluted according to the manufacture's protocol and the concentrations of IL-2, IFN-γ, and IL-4 were measured using a microplate reader (BioTek, Synergy2, VT, USA).

2.10. *Antigen-specific immune response evaluation*

ELISpot assays were performed to evaluate antigen-specific T-cell and B-cell responses. For T-cell analysis, splenocytes isolated from immunized mice were seeded at 2.5×10^5 cells per well into plates precoated with anti-mouse IFN-γ capture antibody and stimulated with the RBD protein. Following incubation and cell removal, biotinylated anti-mouse IFN-γ detection antibody was added for 2 h at room temperature. Plates were washed three times with PBS, followed by the addition of streptavidin-ALP. Spots were developed using the BCIP/NBT-plus substrate and counted using an automated ELISpot reader. For B-cell analysis, splenocytes were seeded into plates precoated with RBD protein (2.5 μg/mL). Following incubation, biotinylated goat anti-mouse IgG antibody was added for 2 h at room temperature. Plates were washed three times with PBS, incubated with streptavidin-ALP, and spots were developed using BCIP/NBT-plus substrate prior to count with the automated ELISpot reader.

2.11. *T-cell subtype polarization analysis*

To examine T-cell subtype polarization, splenocytes were isolated and plated at a density of 2.5×10^5 cells per well. The cells were stimulated with the RBD peptide pool (PP002-A, SinoBiological, Beijing, China) in the presence of 2 μmol/L Monensin. After stimulation, the splenocytes were harvested, washed, and stained with surface antibodies—APC/Cyanine7 anti-CD3, PE/Cyanine7 anti-CD4, and FITC anti-CD8—for 30 min. Subsequently, the cells were fixed and permeabilized using a commercial fixation/permeabilization buffer kit, followed by intracellular staining with APC anti-IL-17, Brilliant Violet 421™ anti-IL-4, and PE anti-IFN-γ antibodies for 1 h. Finally, the stained splenocytes were subjected to flow cytometric analysis.

2.12. Humoral immune response analysis

Healthy BALB/c mice were subcutaneously injected with NS, K8F, Bolus, RC/K8F, RCG/K8F (Wild), RCG/K8F (Delta), RCG/K8F (Omicron). At the predesigned time, blood samples were collected to detect anti-RBD antibodies (IgG, IgM, IgG1, or IgG2b) and evaluate antibody neutralizing effect.

2.13. Antibody production detection

The enzyme-linked immunosorbent assay (ELISA) was carried out to detect anti-RBD antibody production. RBD protein (2 μg/mL) was coated on 96-well plates with high affinity at 4 °C overnight and washed with PBST containing 0.05% Tween-20 twice. 2% BSA in PBS was added to plates and washed plates after 2 h. Then, collected serum samples were serial diluted and incubated in plates at 37 °C for 1 h and afterward washed with PBST twice. The goat anti-mouse IgG(H + L)-HRP, IgM-HRP, IgG1-HRP, and IgG2b-HRP (1:5000 dilution) were incubated in the plates for 1 h, respectively. 100 μL of TMB solution was added to each well and incubated in a dark atmosphere after the plates had been washed. Finally, 50 μL of H_2SO_4 (2 N) was used to stop the reaction and immediately measured the OD value at 450 nm *via* a microplate reader. Endpoint titers were defined as the highest serum dilution at which the OD value exceeded four times the mean OD of sera from PBS-treated control mice.

2.14. Neutralization antibody assay

The collected serum samples were diluted 1:20 and incubated with an equal volume (50 μL) of HRP-RBD solution at 37 °C for 30 min. Then, the mixture was added to 96-well plates precoated with ACE2 protein (1 μg/mL) and incubated at 37 °C. Then, 100 μL of TMB solution was added to each well and incubated in the dark for 15 min after the plates have been washed. Finally, the reaction was terminated by adding 50 μL of H_2SO_4 (2 N), and the OD value was measured at 450 nm using a microplate reader.

2.15. SARS-CoV-2 pseudovirus neutralization test

Pseudovirus neutralization assays were performed as previously described[37]. Briefly, blood samples were collected from immunized mice, and serum was isolated by centrifugation. Sera were diluted proportionately, mixed with SARS-CoV-2 pseudovirus, and incubated for 1 h. The mixtures were then added to Opti-HEK293/ACE2 cells (1×10^4) seeded in a 96-well plate. After 8 h of incubation, the inoculum was removed and replaced with fresh cell culture medium. Following an additional 48 h incubation at 37 °C, firefly luciferase substrate (GenScript) was added to each well. Luminescence was measured using a microplate reader.

2.16. Statistical analysis

Data are reported as mean ± standard deviation (SD). Statistical difference was assessed using one-way ANOVA performed with GraphPad Prism (8.0). $^*P < 0.05$, $^{**}P < 0.01$, and $^{***}P < 0.001$.

3. Results and discussion

3.1. Design of supramolecular hydrogel vaccine

The peptide KFKFEFKFE (KKFE8, Supporting Information Fig. S1) functioned as a smart hydrogelator with good biocompatibility and biodegradability. In aqueous solution, KKFE8 spontaneously self-assembled into filamentous structures (K8F) with a critical assembly concentration of 39.17 μmol/L (Fig. 2A and B, Supporting Information Fig. S2). Circular dichroism (CD) analysis of K8F exhibited a strong negative peak at ∼200 nm, indicative of a predominant random coil structure (Supporting Information Fig. S3). Upon addition of phosphate-buffered saline (PBS), the nanofilaments underwent spontaneous self-assembly into a supramolecular hydrogel (Fig. 2C), mediated by nanofilament entanglements. Rheological characterization confirmed the viscoelastic mechanical properties, the nanofilament solution initially displayed viscoelastic fluid behavior, which underwent a rapid phase transition to a viscoelastic solid state upon introduction of PBS, as evidenced by the storage modulus (G', elastic response) exceeding the loss modulus (G'', viscous response) (Fig. 2D). Furthermore, the nanofilament solution spontaneously transformed into a hydrogel under physiological conditions, demonstrated by in a hydrogel scaffold formed *in situ* 15 min after subcutaneous injection (Supporting Information Fig. S4). H&E-stained sections showed inflammatory cell infiltration near the injection site on Day 1 after implantation; however, this response gradually resolved and was significantly alleviated by Day 20 (Supporting Information Fig. S5A). Differential blood counts—including white blood cells, lymphocytes, monocytes, and neutrophils—showed no significant differences compared to healthy controls (Fig. S5B). Furthermore, inflammatory cytokine levels were comparable to those in control groups, with no significant elevation detected (Fig. S5C and S5D). Together, these results demonstrate the favorable biocompatibility of the K8F hydrogel.

Given the positive charge of K8F, zeta potential measurements revealed a reduction from 46.57 ± 3.51 mV for K8F alone to 39.6 ± 2.5 mV upon RBD binding, with a further decrease to 26.9 ± 0.87 mV following the addition of CpG ODN and GM-CSF to form RCG/K8F (Fig. 2E), collectively demonstrating the electrostatic binding between K8F and vaccine components. The loading content in the RCG/K8F hydrogel was determined to be 0.71% (*w*/*w*) for RBD, 7.12% (*w*/*w*) for CpG ODN, and 0.14% (*w*/*w*) for GM-CSF. Notably, the RCG/K8F composite retained the solution-hydrogel transition capability inherent to K8F (Fig. 2F and Supporting Information Fig. S6). This is due to the addition of anions from PBS that promote filament−filament interactions through charge screening, promoting entanglement of filaments and subsequent hydrogel formation. Furthermore, as confirmed by SEM imaging (Supporting Information Fig. S7), the RCG/K8F hydrogel exhibited a porous network-like structure.

3.2. RCG/K8F hydrogel as a local depot for controlled drug release

To assess the potential of the RCG/K8F hydrogel as a vaccine depot, the release profile of individual vaccine components was investigated *in vitro*. As depicted in Fig. 2G, the hydrogel exhibited the sustained and controlled drug release, with

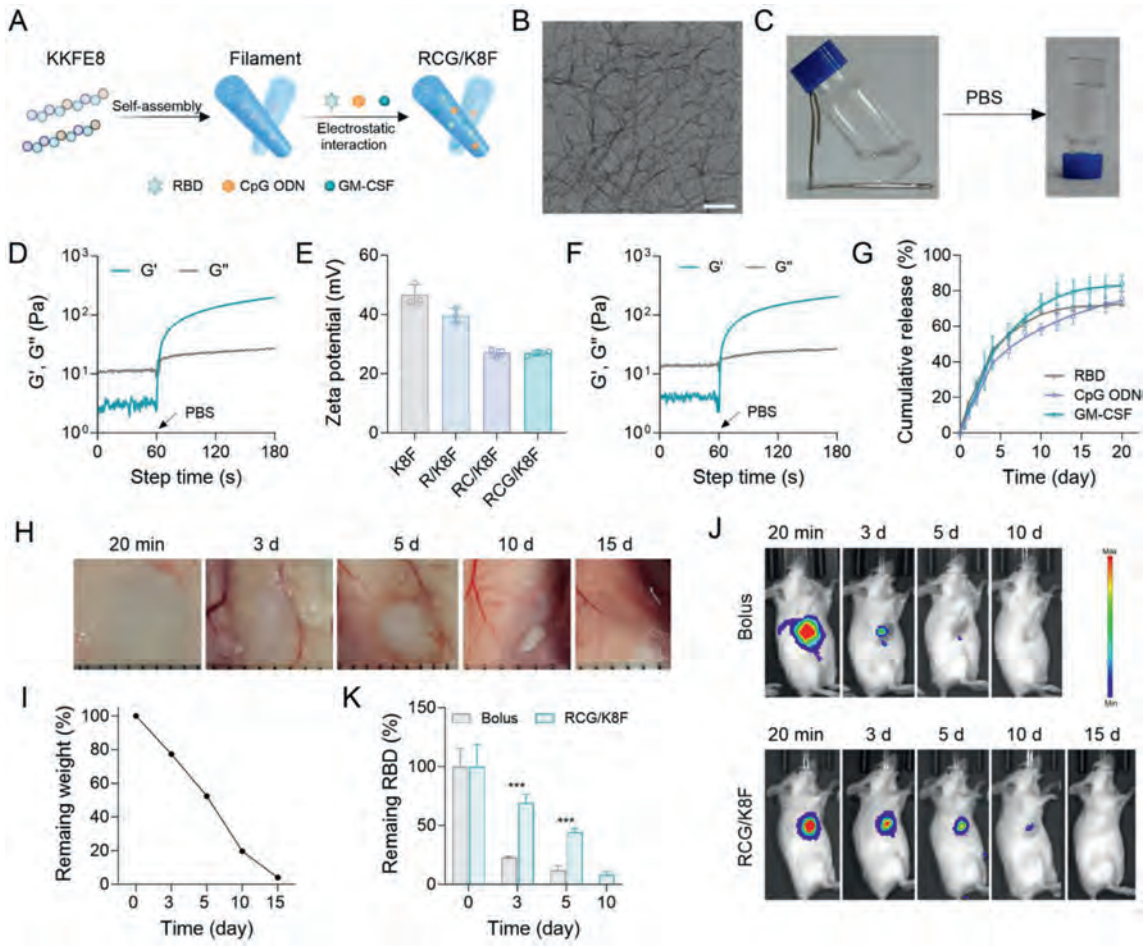

Figure 2 Preparation and characterization of the RCG/K8F hydrogel vaccine. (A) Schematic of RCG/K8F preparation. (B) TEM image of K8F. Scale bar: 200 nm. (C) The solution-to-hydrogel transition of K8F after adding PBS. (D) Rheological properties of K8F determined by time sweep measurements. (E) Zeta potential measurements of K8F, R/K8F, RC/K8F, and RCG/K8F ($n = 3$). (F) Rheological properties of RCG/K8F determined by time sweep measurements. (G) *In vitro* cumulative release of the drug from RCG/K8F hydrogel at different time points ($n = 3$). (H) Representative image of *in vivo* gelation and degradation at different times. (I) Degradation ratio of RCG/K8F hydrogel *in vivo*. (J) *In vivo* distribution and retention of the RBD for Bolus and RCG/K8F groups. (K) Quantification of the fluorescence signal in Bolus and RCG/K8F (Cy5-labelled RBD) groups over time ($n = 3$). Data are expressed as mean ± SD. $^{***}P < 0.001$.

cumulative release of RBD, CpG ODN, and GM-CSF reaching 72.85 ± 1.44%, 75.46 ± 4.24%, and 83.89 ± 4.68%, respectively, at Day 20. In contrast to the rapid release typically associated with nanovaccines[38,39], the RCG/K8F hydrogel achieved an extended drug release profile over 20 days, attributable to its physically cross-linked network and electrostatic interactions with the vaccine components. Encouraged by the sustained drug release performance, we proceeded to characterize *in vivo* hydrogel formation and degradation behavior. Significantly, the RCG/K8F solution demonstrated rapid *in situ* gelation following subcutaneous administration in mice, forming a well-defined spherical hydrogel within 20 min and showing gradual degradation over time (Fig. 2H and I).

To demonstrate the prolonged *in vivo* release of vaccine components, healthy mice were immunized and subsequently imaged by IVIS spectrum. This approach compared the drug distribution and release profile between Bolus components without hydrogel scaffold and RCG/K8F hydrogel groups, with the RBD protein labeled with Cy5. As displayed in Fig. 2J, the fluorescence signal in the Bolus group became negligibly by Day 10 post-injection. In contrast, RCG/K8F group maintained a detectable fluorescence signal for over 10 days. Furthermore, quantitative analysis revealed that the RBD level in the RCG/K8F group was 3.74-fold higher than that of in the Bolus group on Day 5 (Fig. 2K), indicating significantly prolonged antigen retention within the hydrogel. These results indicated that the RCG/K8F served as a local vaccine depot, effectively sustaining the release of antigen *in vivo*.

3.3. *RCG/K8F exhibits favorable in vivo biosafety profile*

To assess the systemic biosafety of RCG/K8F *in vivo*, blood samples and major organs (heart, liver, spleen, lung, and kidney) were collected for comprehensive analysis. Complete blood count results showed that all measured parameters in RCG/K8F-treated mice remained within normal reference ranges and showed no significant differences compared to control mice (Supporting Information Table S1). Serum biochemistry analysis further confirmed that key markers of hepatic and renal function were not significantly altered following RCG/K8F treatment (Supporting

Information Table S2). Together, these hematological and biochemical findings demonstrate the absence of appreciable systemic toxicity after RCG/K8F administration. Additionally, histopathological examination of major organs was performed using H&E staining. Microscopic evaluation revealed normal tissue architecture and cellular morphology in all organs from RCG/K8F-treated mice, which were comparable to those in the control group (Supporting Information Fig. S8). These results are consistent with the blood analyses and collectively indicate that RCG/K8F exhibits a favorable systemic biosafety profile.

3.4. RCG/K8F creates an immune niche to enhance adaptive immunity

To elucidate the dynamic recruitment of innate immune cells mediated by RCG/K8F, we employed multiparametric flow cytometry to systematically analyze its spatially immunomodulatory activity (Fig. 3A and Supporting Information Fig. S9). Quantitative analysis demonstrated that the RCG/K8F formulation significantly enhanced DC recruitment, with an increased percentage of $CD11c^+$ cells (37.1% *vs.* 24.07%) compared to the

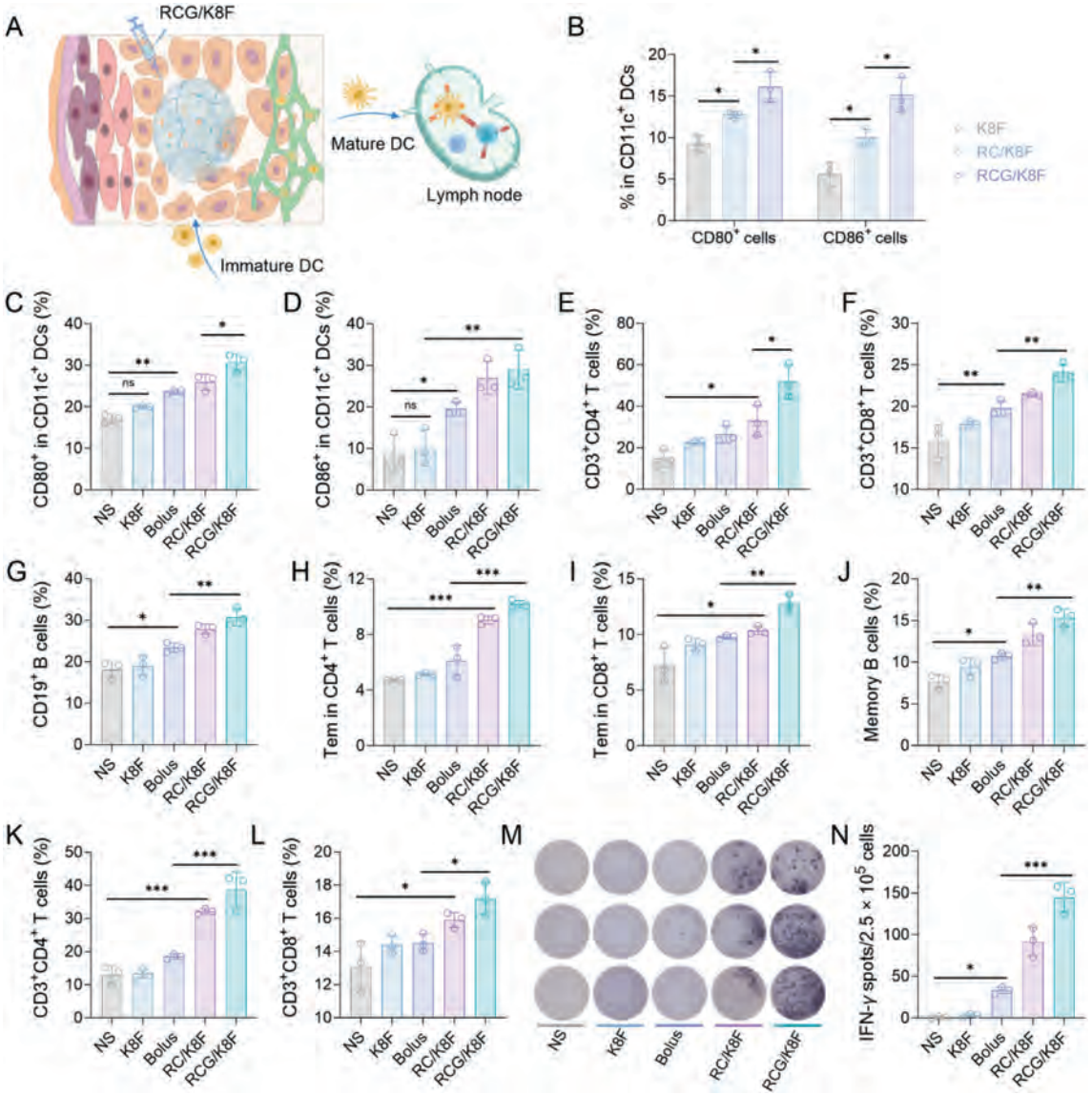

Figure 3 RCG/K8F hydrogel vaccine recruits immature DCs to hydrogel scaffold and enhances cellular immunity. (A) Schematic illustration of the RCG/K8F hydrogel vaccine serving as an immunomodulatory niche to activate DCs and promote their migration to draining lymph nodes. (B) Percentage of $CD11c^+CD80^+$ DCs, and $CD11c^+CD86^+$ DCs within the hydrogel scaffold. Percentage of (C) $CD11c^+CD80^+$ DCs, (D) $CD11c^+CD86^+$ DCs, (E) $CD3^+CD4^+$ T cells, (F) $CD3^+CD8^+$ T cells, and (G) $CD19^+$ B cells in the lymph node 14 days after treatment with NS, K8F, Bolus, RC/K8F, or RCG/K8F. Percentage of (H) $CD4^+$ Tem, (I) $CD8^+$ Tem, and (J) memory B cells in the lymph node. Percentage of (K) $CD3^+CD4^+$ T cells and (L) $CD3^+CD8^+$ T cells in the spleen 28 days following the indicated treatments. (M) Representative ELISpot images showing IFN-γ secretion from splenocytes restimulated with RBD protein. (N) Quantification of IFN-γ^+ spot-forming cells per 2.5×10^5 splenocytes in response to different treatments. Data are expressed as mean ± SD. $^*P < 0.05$, $^{**}P < 0.01$, and $^{***}P < 0.001$. ns, not significant.

blank K8F hydrogel (Supporting Information Fig. S10). Notably, when compared to the RC/K8F group (RBD and CpG ODN-loaded K8F hydrogel), the incorporation of GM-CSF in the RCG/K8F system synergistically promoted DC recruitment, elevating the proportion of $CD11c^+$ cells from 29% to 37.1%. Furthermore, the recruited DCs differentiated into mature DCs under the stimulation of the vaccine (Fig. 3B). Compared with the K8F group, the RCG/K8F group displayed significant increases in $CD11c^+CD80^+$ cells (16.13% *vs.* 9.28%) and $CD11c^+CD86^+$ cells (15.13% *vs.* 5.63%). While DC maturation levels in the K8F group, as measured by surface marker, were comparable to the NS group (Fig. 3C and D), suggesting low immunogenicity of K8F *in vivo*. These surface markers reflect DC maturation, driven by GM-CSF-mediated recruitment of immature DCs to the scaffold and enhanced antigen processing of RBD *via* CpG ODN-stimulated TLR9 signaling, ultimately promoting DCs maturation and enhancing immunogenicity for robust adaptive immunity. Thus, the RCG/K8F created a local immune niche where enriched immune cells triggered the uptake and processing of antigens and transformed into mature DCs, enabling the migration of antigen-laden mature DCs to lymph nodes to activate adaptive immunity after a single injection.

According to the immune response cycle, antigen-loaded DCs migrate to draining lymph nodes to prime antigen-specific $CD3^+CD4^+$ and $CD3^+CD8^+$ T cells, initiating adaptive immune responses[40-42]. As shown in Fig. 3C and D, RCG/K8F potentiated DC activation 14 days post-immunization compared to the Bolus group, evidenced by increased percentages of $CD11c^+CD80^+$ cells (30.67% *vs.* 23.6%) and $CD11c^+CD86^+$ cells (29% *vs.* 19.53%). The enhanced antigen-presenting capacity of these mature DCs was functionally validated by their superior ability to prime naive T cells. Flow cytometry confirmed that RCG/K8F vaccination significantly boosted activation of both $CD3^+CD4^+$ (51.8% *vs.* 26.57%) and $CD3^+CD8^+$ T cells (24.07% *vs.* 19.77%) compared to conventional Bolus immunization. Specifically, the proportion of $CD3^+CD4^+$ T cells and $CD3^+CD8^+$ T cells was increased in mice receiving the RCG/K8F compared to the RC/K8F group on Day 14 (Fig. 3E and F). Furthermore, quantitative analysis also revealed significantly increased $CD19^+$ B cell densities in the RCG/K8F (30.73%) *versus* the Bolus (23.43%) 14 days after immunization (Fig. 3G). Collectively, these findings suggested that RCG/K8F created an immune niche that enhanced adaptive immunity.

Encouraged by the enhanced immunity of RCG/K8F, we further assessed immune activation 28 days after a single vaccination to evaluate its potential to induce durable immunity. RCG/K8F effectively maintained the activation of DCs and induced long-term cellular immune responses, as demonstrated on activation of $CD3^+CD4^+$ T cells and $CD3^+CD8^+$ T cells (Supporting Information Fig. S11A−S11D). Following a single vaccination with RCG/K8F, the percentage of $CD3^+CD4^+$ T cells was 3.32-times higher than in the NS group and 1.48-fold higher than in the Bolus groups (Fig. S11C). Sustained immune activation was further demonstrated by the increase in $CD3^+CD8^+$ T cells (Fig. S11D), which were 1.3- and 1.16-fold the percentage observed in the NS and Bolus groups, respectively. Complementing this, RCG/K8F also produced a significantly higher percentage of $CD19^+$ B cells (28.97%) than Bolus (20%) at Day 28 (Fig. S11E), with this expansion strongly correlating with antibody production, indicating potentiated humoral immunity. Furthermore, vaccination with RCG/K8F markedly increased the frequencies of effector memory T cells (Tem) among both $CD4^+$ and $CD8^+$ T cell subsets, as well as memory B cells in the lymph nodes (Fig. 3H−J). Upon antigen re-exposure, these memory B cells can undergo rapid expansion and differentiation into antibody-secreting cells, thereby playing a critical role in sustained antiviral immunity. Collectively, these results indicated that RCG/K8F induced long-lasting cellular immune responses.

Furthermore, RCG/K8F activated systemic immune responses as evidenced by the promotion of immune cell activation and proliferation in the spleen. By Day 14 post-vaccination, RCG/K8F-immunized mice showed proliferation indices 1.75-fold higher ($CD3^+CD4^+$ T cells) and 1.32-fold higher ($CD3^+CD8^+$ T cells) than the Bolus group (Fig. S11F and S11G). Remarkably, this immunocompetence was sustained through Day 28, with $CD3^+CD4^+$ T cell frequencies rising from 12.97% in the NS group to 38.63% in the RCG/K8F group (Fig. 3K). Concurrently, $CD3^+CD8^+$ T cell populations were 1.31 times higher than in the NS group and 1.19 times higher than in the Bolus group (Fig. 3L). These quantitative findings demonstrated that the RCG/K8F platform induced durable adaptive immunity following a single administration, outperforming traditional vaccination paradigms in maintaining lymphocyte activation kinetics.

3.5. RCG/K8F activates robust antigen-specific immune responses

To evaluate antigen-specific immune activation, splenocytes from mice immunized with RCG/K8F were analyzed using ELISpot assays. After stimulation with the RBD protein, representative well images showed IFN-γ spot formation only in groups immunized with formulations containing the RBD antigen (Fig. 3M). Notably, the RCG/K8F group exhibited a significantly higher number of IFN-γ spots, which was 4.38-fold more than that in the Bolus group, indicating that RCG/K8F enhances antigen-specific T cell immune response (Fig. 3N). Furthermore, antigen-specific B cell responses were also assessed using an RBD-coated ELISpot assay. A substantial number of RBD-specific IgG spots was observed in the RCG/K8F group (Supporting Information Fig. S12A). Quantitative analysis confirmed that the number of spots was 2.96-fold higher than in the Bolus group (Fig. S12B). These results demonstrate that RCG/K8F vaccination elicits a potent antigen-specific B-cell response, conducive to antibody production against viral infection.

3.6. RCG/K8F hydrogel vaccine induces long-term and robust humoral immune responses

To assess the RCG/K8F hydrogel vaccine's ability to generate humoral immunity against infectious disease, the blood samples from BALB/c mice were collected to analyze antibody subclasses produced *via* enzyme-linked immunosorbent assay (ELISA) (Fig. 4A). This analysis specifically quantified IgM (the primary antibody isotype generated during initial antigen exposure prior to class switching) and IgG (the dominant isotype mediating secondary responses post-switching), which serve as temporal biomarkers of B cell activation and affinity maturation[43]. RCG/K8F vaccination induced higher IgM responses than Bolus group, with optical density (OD) values 2.61-fold higher on Day 14 and 1.4-fold higher on Day 28 (Fig. 4B and Supporting Information Fig. S13). Additionally, RCG/K8F showed exceptional antibody persistence, with OD value increasing from 0.08 to 1.75 at a 1:80 serum dilution 112 days after immunization (Fig. 4C−E). With increasing dilution, robust and durable IgG responses against RBD protein remained highly effective in the RCG/K8F groups even at

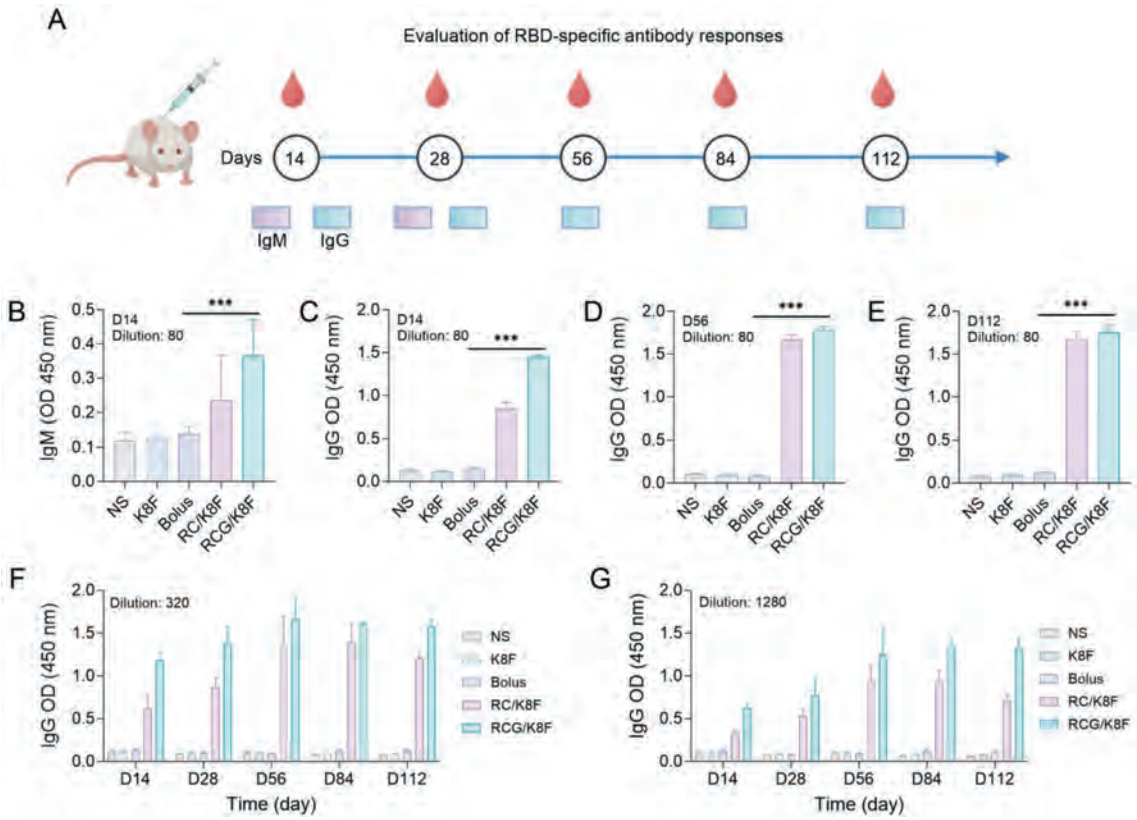

Figure 4 RCG/K8F hydrogel vaccine induces long-term humoral immunity after a single vaccination. (A) Schematic timeline of blood sample collection for assessing anti-RBD antibody responses. (B) RBD-specific IgM levels in mouse sera 14 days post-treatment with NS, K8F, Bolus, RC/K8F, or RCG/K8F. RBD-specific IgG levels measured at (C) 14 days, (D) 56 days, and (E) 112 days post-vaccination. RBD-specific IgG levels measured at (F) 1:320 (G) 1:1280 serum dilution at the indicated time points. Data are expressed as mean ± SD. ***$P < 0.001$.

high serum dilutions (Fig. 4F and G). Furthermore, anti-RBD IgG titer was quantitatively assessed (Supporting Information Fig. S14A). The RCG/K8F group maintained significantly elevated anti-RBD IgG titers throughout the 112-day observation period, whereas titers in both K8F and Bolus groups remained below the limit of quantification. Taken together, these results indicated that RCG/K8F induced potent and long-term humoral immune responses.

To gain a deeper understanding of the immunostimulatory effect of the RCG/K8F on adaptive immune responses, we quantified the production level of IgG subtypes, specially IgG1 and IgG2b. IgG1 represented Th2-dominated immune responses, whereas IgG2b indicated Th1-directed immune responses[44,45]. The RCG/K8F elicited mixed immune responses through the production of both IgG1 (Fig. 5A—C) and IgG2b antibodies (Fig. 5D—F), suggesting that immunization promoted humoral responses with mixed Th1/Th2 phenotype. The increased production of IgG1 and IgG2b antibody was further supported by the higher OD values in the RCG/K8F group, which was 12.98- and 8.83-fold than that of in the Bolus group 14 days post-immunization, respectively. Quantitative analyses confirmed sustained immunogenicity of RCG/K8F at 112 days post-vaccination (Fig. S14B and S14C). Superior anti-RBD IgG1 and IgG2b titers persisted in the RCG/K8F group at this timepoint, in sharp contrast to the K8F and Bolus groups where both IgG subtypes remained below the limit of quantification. Additionally, cytokine profiles associated with Th1/Th2 responses were quantified in serum at Days 14 and 28 post-immunization. Th1 cells secrete interferon-γ (IFN-γ) and interleukin-2 (IL-2) that instruct B cells to produce opsonizing antibodies (IgG2b) that stimulate macrophage clearance of intracellular pathogens; whereas Th2 cells produce interleukin-4 (IL-4) that instruct B cells to secrete neutralizing antibodies (IgG1) for humoral protection against extracellular pathogens[46]. Sera from RCG/K8F-immunized mice both induced Th1/Th2 immune responses through increased IFN-γ, IL-2, and IL-4 secretion (Fig. 5G—J). Notably, robust cytokine levels were sustained at Day 28 (Supporting Information Fig. S15), suggesting that RCG/K8F elicited a mixed Th1/Th2 immune response over a prolonged period.

To further investigate T-cell subtype polarization, $CD4^+$ and $CD8^+$ T-cell responses in splenocytes following stimulation with the RBD peptide pool were analyzed by flow cytometry. Compared to the NS group, RCG/K8F vaccination induced higher frequencies of IFN-γ and IL-4 producing $CD4^+$ and $CD8^+$ T cells, while no significant difference was observed in IL-17 production (Supporting Information Fig. S16). Notably, as shown in Fig. 5K and L, RCG/K8F elicited significantly greater populations of IFN-γ producing (Th1) $CD4^+$ and $CD8^+$ T cells compared to those producing IL-4 (Th2) or IL-17 (Th17), indicating a Th1-biased cellular immune response. This bias toward Th1 polarization may be attributed to the adjuvant CpG ODN, which skews the immune milieu toward a Th1-type response[47,48].

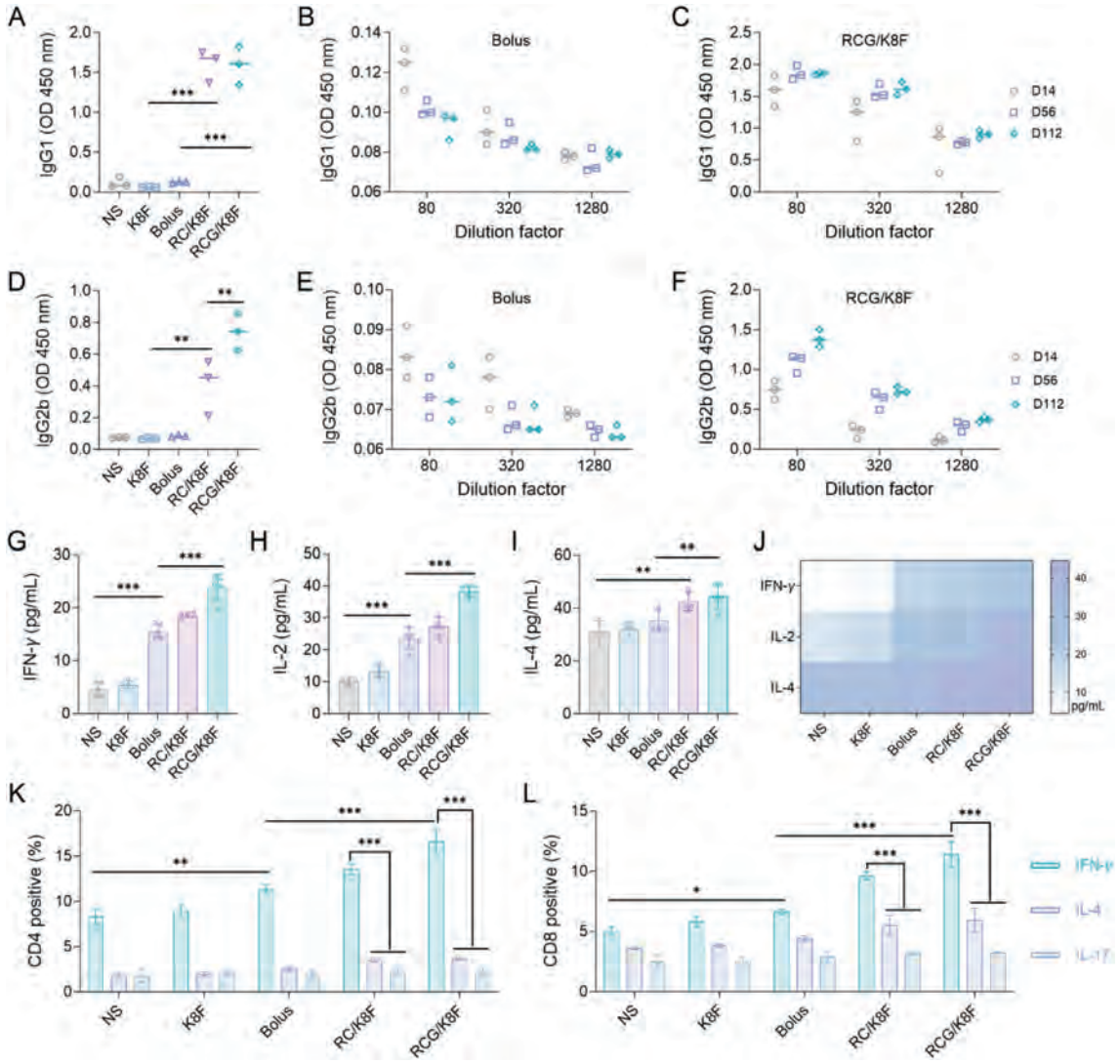

Figure 5 RCG/K8F hydrogel vaccine elicits Th1 and Th2 immune response. (A) RBD-specific IgG1 antibody levels after treatment of mice with NS, K8F, Bolus, RC/K8F, or RCG/K8F ($n = 3$). RBD-specific IgG1 antibody levels in (B) Bolus and (C) RCG/K8F immunized mice on Days 14, 56, and 112 ($n = 3$). (D) RBD-specific IgG2b antibody levels after treatment of mice with NS, K8F, Bolus, RC/K8F, and RCG/K8F ($n = 3$). RBD-specific IgG2b antibody levels in (E) Bolus and (F) RCG/K8F immunized mice on Days 14, 56, and 112 ($n = 3$). Cytokine levels of (G) IFN-γ, (H) IL-2, and (I) IL-4 14 days after immunization mice with NS, K8F, Bolus, RC/K8F, or RCG/K8F ($n = 5$). (J) Cytokine heatmap of IFN-γ, IL-2, and IL-4 after mice receiving the indicated treatments after 14 days. (K) Frequency of IFN-γ, IL-4, or IL-17 producing $CD4^+$ T cells and (L) $CD8^+$ T cells in RBD peptide-stimulated splenocytes. Data are expressed as mean ± SD. $^*P < 0.05$, $^{**}P < 0.01$, and $^{***}P < 0.001$.

3.7. RCG/K8F hydrogel vaccine elicits durable and enhanced neutralizing effect

SARS-CoV-2 expresses multiple protein targets, among which the RBD protein expressed on spike protein is directly interacted with the angiotensin-converting enzyme 2 (ACE2) on host cells (Fig. 6A and B), mediating virus absorption, fusion, and entry into host cells[49-53]. Due to these pathophysiological pathways, blocking the interaction between the RBD protein and ACE2 is essential to prevent SARS-CoV-2 infection in host cells[54,55]. The competitive ELISA strategy was used to assess whether sera from immunized mice could inhibit these interactions (Fig. 6C). As shown in Fig. 6D, sera from mice immunized with RCG/K8F significantly neutralized the interaction between RBD and ACE2. At 14 days post-vaccination, the inhibition ratio in the RCG/K8F group (50.72%) was significantly higher than that observed in the Bolus (14.26%) and RC/K8F (33.23%) groups. Notably, the inhibition rate showed an increasing trend over time, reaching 80.71% at 56 days and 80.4% at 112 days after RCG/K8F immunization (Fig. 6E and F), consistent with the sustained antibody responses previously described. Thus, mice vaccinated with the RCG/K8F induced the long-term production of antibodies capable of blocking the interaction between RBD and ACE2, thereby potentiating viral prevention.

Furthermore, a pseudovirus assay was performed to evaluate the neutralizing effect of the RCG/K8F hydrogel vaccine against SARS-CoV-2. Luciferase-tagged Opti-HEK293/ACE2 cells expressing the ACE2 receptor can be infected by the pseudovirus through the spike glycoproteins exposed on the virion surface[56,57].

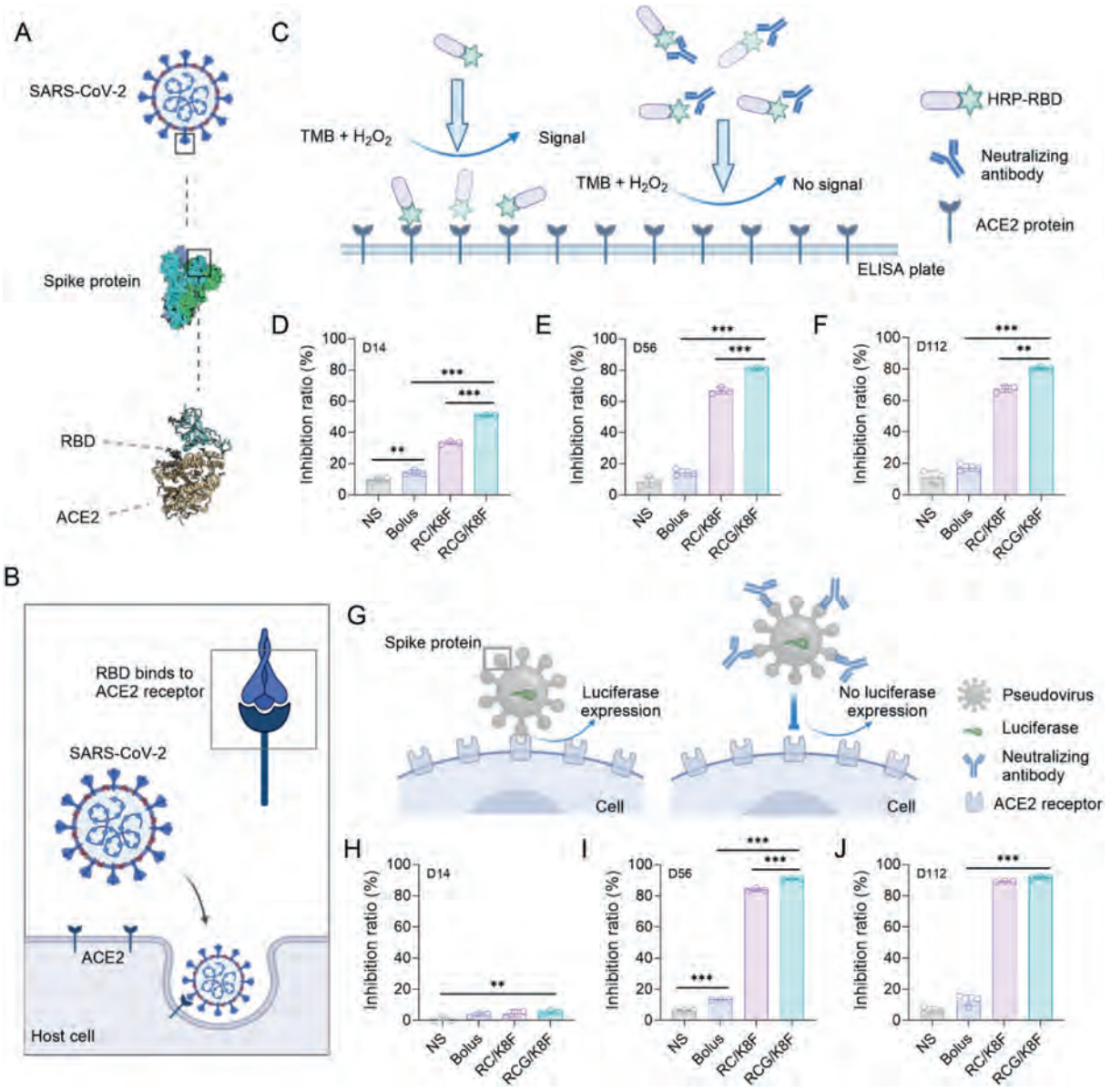

Figure 6 RCG/K8F hydrogel vaccine induces durable and enhanced neutralization potential. (A) Structure of the RBD in complex with the ACE2 receptor. (B) Mechanistic illustration of RBD interaction with ACE2 during host cell invasion. Reproduced with permission from BioRender. (C) Schematic illustration of competitive ELISA-based surrogate virus neutralization test. Inhibition ratios in the NS, Bolus, RC/K8F, and RCG/K8F groups on (D) 14, (E) 56, and (F) 112 days post-immunization ($n = 3$). (G) Schematic illustration of the pseudovirus-based neutralization test. Inhibition ratios in the NS, Bolus, RC/K8F, and RCG/K8F groups on (H) 14, (I) 56, and (J) 112 days post-immunization *via* pseudovirus assay ($n = 3$). Data are expressed as mean ± SD. $^{**}P < 0.01$, and $^{***}P < 0.001$.

Neutralizing antibodies produced in the serum of immunized mice bind to surface spike glycoproteins, thereby inhibiting viral attachment (Fig. 6G). Quantitative pseudovirus neutralization assays demonstrated the RCG/K8F hydrogel vaccine's superior and sustained antiviral efficacy (Fig. 6H−J). Compared with the NS group (inhibition rate below 10%), the pseudovirus neutralizing antibody capacity against SARS-CoV-2 was 90.92% and 91.57% after 56 and 112 days of vaccination with RCG/K8F, respectively. These results demonstrated that RCG/K8F effectively neutralized the interaction between the spike protein and the ACE2 receptor, suggesting its capability to efficiently prevent SARS-CoV-2 infection.

3.8. RCG/K8F hydrogel vaccine elicits superior immune response over conventional vaccination

Given the robust adaptive immunity induced by RCG/K8F, we further compared the immune responses it elicited with those induced by a conventional vaccine (RBD formulated with Alum adjuvant). Mice received either RBD + Alum *via* prime-boost immunization or a single dose of RCG/K8F (Supporting Information Fig. S17A). Following a single immunization, RCG/K8F significantly enhanced DCs activation and initiated stronger adaptive immune responses compared to RBD + Alum (Fig. S17B−S17F). The proportion of $CD4^+$ T cells in the lymph

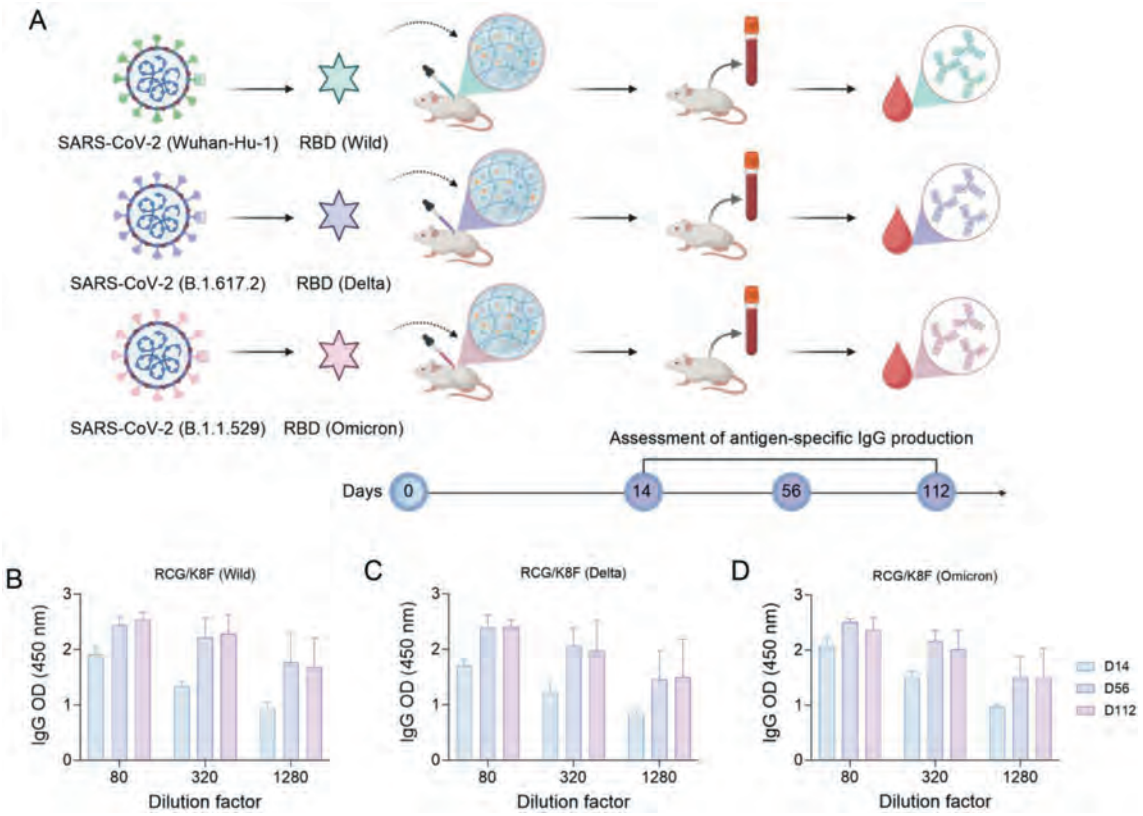

Figure 7 RBD-specific IgG antibody production *in vivo*. (A) Evaluation of variant-specific IgG protection mediated by RCG/K8F hydrogel-based antigen delivery. RBD-specific IgG antibody production kinetics in mice receiving (B) RCG/K8F (Wild RBD), (C) RCG/K8F (Delta RBD), and (D) RCG/K8F (Omicron RBD) on 14, 56, and 112 days.

nodes increased from 37.8% (RBD + Alum) to 58.7% (RCG/K8F). Similarly, the percentage of $CD8^+$ T cells rose from 18.77% to 22.43%. Additionally, RCG/K8F enhanced B cell activation, achieving a level 1.4-fold higher than that in the RBD + Alum group. Together, these results demonstrate that RCG/K8F elicits a more robust cellular immune response than prime-boost immunization with RBD + Alum.

Additionally, we investigated the differences in the humoral immune responses between the groups. RCG/K8F generated significantly higher RBD-specific IgG titers in serum compared to the RBD + Alum group (Fig. S17G). Importantly, the elevated IgG levels correlated with enhanced functional activity. As revealed in neutralization assays, a significantly higher inhibition rate for RCG/K8F (57.79%) than for RBD + Alum (32.96%) (Fig. S17H). The improved neutralizing capacity of RCG/K8F suggests its potential to provide superior protection, underscoring its advantage over conventional Alum-adjuvanted RBD vaccines in eliciting humoral immunity.

3.9. RCG/K8F hydrogel serves as a universal vaccine platform for orchestrating antigen-specific adaptive immunity

To address pandemic scale challenges posed by rapid viral evolution and pathogen diversification, we systematically investigated the pan-variant immunization capacity of an engineered supramolecular hydrogel vaccine platform. Antigenic components screened from the SARS-CoV-2 variant include Wild RBD (Wuhan-Hu-1), Delta RBD (B.1.617.2), and Omicron RBD (B.1.1.529) were individually constructed into the RCG/K8F hydrogel to determine antibody production by ELISA assay (Fig. 7A). The RCG/K8F hydrogel platform exhibited superior humoral immunogenicity over time, maintaining detectable antigen-specific IgG generation even at a serum dilution of 1:1280 (Fig. 7B−D). Crucially, this platform demonstrated antigen-specific antibody induction capabilities when functionalized with distinct SARS-CoV-2 RBD variants (Wild RBD (Wuhan-Hu-1), Delta RBD (B.1.617.2), or Omicron RBD (B.1.1.529)). All formulations exhibited sustained antibody persistence, with high IgG levels maintained up to Day 112 post-vaccination, highlighting the versatility of the RCG/K8F hydrogel vaccine in accommodating varying antigenic components for durable antigen-specific antibody generation. These findings suggested that the RCG/K8F hydrogel could serve as a universal vaccine platform by incorporating mutated RBD antigens to combat emerging SARS-CoV-2 variants.

4. Conclusions

In this work, we developed a self-assembling peptide-based supramolecular hydrogel vaccine to create a localized immune niche, demonstrating its exceptional efficacy in eliciting durable and potent immunity against infectious diseases. We showed that the *in situ* formed supramolecular hydrogel vaccine, RCG/K8F, acted as a depot for antigens and adjuvants while recruiting antigen-presenting DCs to accumulate within the scaffold. Facilitated by adjuvants, the DCs undergo enhanced antigen processing

and presentation, establishing an immunologically active niche that induces robust B cell and T cell responses. Furthermore, we observed sustained IgG antibody production for 112 days, highlighting the potential of the supramolecular hydrogel vaccine to provide durable immunological protection with a single vaccination. Notably, in a SARS-CoV-2 infectious disease model, the RCG/K8F hydrogel vaccine effectively neutralized the interaction between the spike protein and the ACE2 receptor, demonstrating its potential to efficiently inhibit SARS-CoV-2 infection. Collectively, these findings suggest that this localized supramolecular hydrogel vaccine can elicit durable and enhanced immunity against infectious diseases.

Acknowledgments

This work is supported by National Natural Science Foundation of China (Nos. 82104076 and 82473851); National Key Research and Development Program of China (No. 2022YFC3501905); Science and Technology Commission of Shanghai Municipal (No. 22S21902400); Key Project at Central Government Level: the Ability Establishment of Sustainable Use for Valuable Chinese Medicine Resources (No. 2060302) and Medicine Engineering Joint Foundation of Shanghai Jiao Tong University (Nos. YG2025ZD22, YG2022QN025, and YG2022QN050, China).

Author contributions

Qi Shang: conceptualization, experiments and collected the data, data analysis, visualization, writing-original draft; Chenwei Jiang: methodology, visualization, writing-original draft; Xiaolong Wang: methodology, visualization; Mingmei Guo, Jing Liu, Zhedong Jin: experiments and collected the data, data analysis, validation; Yunsheng Yuan: supervision, writing-review & editing; Feihu Wang: conceptualization, funding acquisition, writing-review & editing.

Conflicts of interest

The authors declare no conflicts of interest.

Appendix A. Supporting information

Supporting information to this article can be found online at https://doi.org/10.1016/j.apsb.2025.09.014.

References

1. Ortega-Rivera OA, Shin MD, Chen A, Beiss V, Moreno-Gonzalez MA, Lopez-Ramirez MA, et al. Trivalent subunit vaccine candidates for COVID-19 and their delivery devices. *J Am Chem Soc* 2021;**143**:14748−65.
2. Wu Y, Jia XY, Wu NM, Zhang XH, Wu Y, Liu Y, et al. Boosting with Omicron-specific mRNA vaccine or historical SARS-CoV-2 vaccines elicits discriminating immune responses against Omicron variants. *Acta Pharm Sin B* 2025;**15**:947−62.
3. Yi DR, Zhang YX, Wang J, Liu Q, Ma L, Li QJ, et al. Protection efficacy of mRNA-based SARS-CoV-2 variant vaccine in non-human primates. *Acta Pharm Sin B* 2025;**15**:934−46.
4. Hulme WJ, Horne EMF, Parker EPK, Keogh RH, Williamson EJ, Walker V, et al. Comparative effectiveness of BNT162b2 *versus* mRNA-1273 COVID-19 vaccine boosting in England: matched cohort study in OpenSAFELY-TPP. *BMJ* 2023;**380**:e072808.
5. Lustig Y, Gonen T, Meltzer L, Gilboa M, Indenbaum V, Cohen C, et al. Superior immunogenicity and effectiveness of the third compared to the second BNT162b2 vaccine dose. *Nat Immunol* 2022;**23**:940−6.
6. Mahumud RA, Alam K, Keramat SA, Ormsby GM, Dunn J, Gow J. Cost-effectiveness evaluations of the 9-Valent human papillomavirus (HPV) vaccine: evidence from a systematic review. *PLoS One* 2020;**15**:e0233499.
7. Kantoff PW, Higano CS, Shore ND, Berger ER, Small EJ, Penson DF, et al. Sipuleucel-T immunotherapy for castration-resistant prostate cancer. *N Engl J Med* 2010;**363**:411−22.
8. Guo Y, Lei K, Tang L. Neoantigen vaccine delivery for personalized anticancer immunotherapy. *Front Immunol* 2018;**9**:1499.
9. Hou YY, Chen M, Bian Y, Zheng X, Tong RS, Sun X. Advanced subunit vaccine delivery technologies: from vaccine cascade obstacles to design strategies. *Acta Pharm Sin B* 2023;**13**:3321−38.
10. Roth GA, Picece V, Ou BS, Luo W, Pulendran B, Appel EA. Designing spatial and temporal control of vaccine responses. *Nat Rev Mater* 2022;**7**:174−95.
11. Mabrouk MT, Huang WC, Martinez-Sobrido L, Lovell JF. Advanced materials for SARS-CoV-2 vaccines. *Adv Mater* 2022;**34**:e2107781.
12. Chaudhary N, Weissman D, Whitehead KA. mRNA vaccines for infectious diseases: principles, delivery and clinical translation. *Nat Rev Drug Discov* 2021;**20**:817−38.
13. Liu XQ, Li YH, Wang ZF, Cao SC, Huang WJ, Yuan L, et al. Safety and superior immunogenicity of heterologous boosting with an RBD-based SARS-CoV-2 mRNA vaccine in Chinese adults. *Cell Res* 2022;**32**:777−80.
14. Minervina AA, Pogorelyy MV, Kirk AM, Crawford JC, Allen EK, Chou CH, et al. SARS-CoV-2 antigen exposure history shapes phenotypes and specificity of memory $CD8^+$ T cells. *Nat Immunol* 2022;**23**:781−90.
15. Yang W, Cao JW, Cheng H, Chen L, Yu MH, Chen Y, et al. Nanoformulations targeting immune cells for cancer therapy: mRNA therapeutics. *Bioact Mater* 2023;**23**:438−70.
16. Uddin MN, Roni MA. Challenges of storage and stability of mRNA-based COVID-19 vaccines. *Vaccines (Basel)* 2021;**9**:1033.
17. Garcia-Beltran WF, Lam EC, St Denis K, Nitido AD, Garcia ZH, Hauser BM, et al. Multiple SARS-CoV-2 variants escape neutralization by vaccine-induced humoral immunity. *Cell* 2021;**184**:2372−83.
18. Ali OA, Huebsch N, Cao L, Dranoff G, Mooney DJ. Infection-mimicking materials to program dendritic cells *in situ*. *Nat Mater* 2009;**8**:151−8.
19. Eggermont LJ, Paulis LE, Tel J, Figdor CG. Towards efficient cancer immunotherapy: advances in developing artificial antigen-presenting cells. *Trends Biotechnol* 2014;**32**:456−65.
20. Phuengkham H, Song C, Um SH, Lim YT. Implantable synthetic immune niche for spatiotemporal modulation of tumor-derived immunosuppression and systemic antitumor immunity: postoperative immunotherapy. *Adv Mater* 2018;**30**:e1706719.
21. Li Q, Zhao ZP, Qin XH, Zhang MZ, Du Q, Li ZH, et al. A checkpoint-regulatable immune niche created by injectable hydrogel for tumor therapy. *Adv Funct Mater* 2021;**31**:2104630.
22. Phuengkham H, Ren L, Shin IW, Lim YT. Nanoengineered immune niches for reprogramming the immunosuppressive tumor microenvironment and enhancing cancer immunotherapy. *Adv Mater* 2019;**31**:e1803322.
23. Shang Q, Su Y, Leslie F, Sun MJ, Wang FH. Advances in peptide-drug conjugate-based supramolecular hydrogel systems for local drug delivery. *Med Drug Disc* 2022;**14**:100125.
24. Wang F, Su H, Lin R, Chakroun RW, Monroe MK, Wang Z, et al. Supramolecular tubustecan hydrogel as chemotherapeutic carrier to improve tumor penetration and local treatment efficacy. *ACS Nano* 2020;**14**:10083−94.
25. Cai Y, Zheng C, Xiong F, Ran W, Zhai Y, Zhu HH, et al. Recent progress in the design and application of supramolecular peptide hydrogels in cancer therapy. *Adv Healthcare Mater* 2021;**10**:e2001239.

26. Zhang S. Fabrication of novel biomaterials through molecular self-assembly. *Nat Biotechnol* 2003;**21**:1171−8.
27. Davide MM, Wonmuk H, Douglas AL, Shuguang Z, Roger DK. Left-handed helical ribbon intermediates in the self-assembly of a â-sheet peptide. *Nano Lett* 2001;**2**:295−9.
28. Zhang J, Chen C, Li A, Jing WQ, Sun P, Huang XY, et al. Immunostimulant hydrogel for the inhibition of malignant glioma relapse post-resection. *Nat Nanotechnol* 2021;**16**:538−48.
29. Elsawy MA, Wychowaniec JK, Castillo Diaz LA, Smith AM, Miller AF, Saiani A. Controlling doxorubicin release from a peptide hydrogel through fine-tuning of drug−peptide fiber interactions. *Biomacromolecules* 2022;**23**:2624−34.
30. Shang Q, Dong YB, Su Y, Leslie F, Sun MJ, Wang FH. Local scaffold-assisted delivery of immunotherapeutic agents for improved cancer immunotherapy. *Adv Drug Deliv Rev* 2022;**185**: 114308.
31. Wang FH, Su H, Wang ZY, Anderson CF, Sun XR, Wang H, et al. Supramolecular filament hydrogel as a universal immunomodulator carrier for immunotherapy combinations. *ACS Nano* 2023;**17**: 10651−64.
32. Wang FH, Su H, Xu DQ, Dai WB, Zhang WJ, Wang ZY, et al. Tumour sensitization *via* the extended intratumoural release of a STING agonist and camptothecin from a self-assembled hydrogel. *Nat Biomed Eng* 2020;**4**:1090−101.
33. Wang FH, Xu DQ, Su H, Zhang WJ, Sun XR, Monroe MK, et al. Supramolecular prodrug hydrogelator as an immune booster for checkpoint blocker-based immunotherapy. *Sci Adv* 2020;**6**: eaaz8985.
34. Wang F, Su H, Xu D, Monroe MK, Anderson CF, Zhang W, et al. Therapeutic supramolecular tubustecan hydrogel combined with checkpoint inhibitor elicits immunity to combat cancer. *Biomaterials* 2021;**279**:121182.
35. Anderson CF, Chakroun RW, Grimmett ME, Domalewski CJ, Wang F, Cui H. Collagen-binding peptide-enabled supramolecular hydrogel design for improved organ adhesion and sprayable therapeutic delivery. *Nano Lett* 2022;**22**:4182−91.
36. Wang FH, Huang Q, Su H, Sun MJ, Wang ZY, Chen ZQ, et al. Self-assembling paclitaxel-mediated stimulation of tumor-associated macrophages for postoperative treatment of glioblastoma. *Proc Natl Acad Sci U S A* 2023;**120**:e2204621120.
37. Mao SH, Li SY, Zhang YX, Long LX, Peng JF, Cao YY, et al. A highly efficient needle-free-injection delivery system for mRNA-LNP vaccination against SARS-CoV-2. *Nano Today* 2023;**48**: 101730.
38. Liu MQ, Feng Y, Lu YG, Huang RQ, Zhang Y, Zhao YA, et al. Lymph-targeted high-density lipoprotein-mimetic nanovaccine for multi-antigenic personalized cancer immunotherapy. *Sci Adv* 2024;**10**: eadk2444.
39. Yi YF, Yu M, Li W, Zhu DW, Mei L, Ou MT. Vaccine-like nanomedicine for cancer immunotherapy. *J Control Release* 2023;**355**: 760−78.
40. Lei H, Alu A, Yang JY, He X, He C, Ren WY, et al. Cationic cross-linked carbon dots-adjuvanted intranasal vaccine induces protective immunity against Omicron-included SARS-CoV-2 variants. *Nat Commun* 2023;**14**:2678.
41. Zhang JX, Cao JH, Wang LC, Li ST, Meng FQ, Liang X, et al. Neoantigen sequestrated autophagosomes as therapeutic cancer vaccines. *J Control Release* 2024;**376**:369−81.
42. Li QQ, Shi ZQ, Zhang F, Zeng WW, Zhu DW, Mei L. Symphony of nanomaterials and immunotherapy based on the cancer−immunity cycle. *Acta Pharm Sin B* 2022;**12**:107−34.
43. Gale EC, Powell AE, Roth GA, Meany EL, Yan J, Ou BS, et al. Hydrogel-based slow release of a receptor-binding domain subunit vaccine elicits neutralizing antibody responses against SARS-CoV-2. *Adv Mater* 2021;**33**:e2104362.
44. Vinuesa CG, Tangye SG, Moser B, Mackay CR. Follicular B helper T cells in antibody responses and autoimmunity. *Nat Rev Immunol* 2005; **5**:853−65.
45. Wan DD, Bai ZY, Zhang Y, Chen L, Que HY, Lan TX, et al. Simultaneous enhancement of cellular and humoral immunity by the lymph node-targeted cholesterolized TLR7 agonist liposomes. *Acta Pharm Sin B* 2024;**14**:4577−90.
46. Romagnani S. Th1/Th2 cells. *Inflamm Bowel Dis* 1999;**5**:285−94.
47. Klinman DM. Immunotherapeutic uses of CpG oligodeoxynucleotides. *Nat Rev Immunol* 2004;**4**:248−57.
48. Pradhan P, Qin H, Leleux JA, Gwak D, Sakamaki I, Kwak LW, et al. The effect of combined IL10 siRNA and CpG ODN as pathogenmimicking microparticles on Th1/Th2 cytokine balance in dendritic cells and protective immunity against B cell lymphoma. *Biomaterials* 2014;**35**: 5491−504.
49. Xu K, Gao P, Liu SY, Lu S, Lei WW, Zheng TY, et al. Protective prototype-Beta and Delta-Omicron chimeric RBD-dimer vaccines against SARS-CoV-2. *Cell* 2022;**185**:2265−78.
50. Huang X, Kon E, Han XX, Zhang XC, Kong N, Mitchell MJ, et al. Nanotechnology-based strategies against SARS-CoV-2 variants. *Nat Nanotechnol* 2022;**17**:1027−37.
51. Atalis A, Keenum MC, Pandey B, Beach A, Pradhan P, Vantucci C, et al. Nanoparticle-delivered TLR4 and RIG-I agonists enhance immune response to SARS-CoV-2 subunit vaccine. *J Control Release* 2022;**347**:476−88.
52. Tu B, Gao YR, An XR, Wang HY, Huang YZ. Localized delivery of nanomedicine and antibodies for combating COVID-19. *Acta Pharm Sin B* 2022;**13**:1828−46.
53. Lam JH, Khan AK, Cornell TA, Chia TW, Dress RJ, Yeow WWW, et al. Polymersomes as stable nanocarriers for a highly immunogenic and durable SARS-CoV-2 spike protein subunit vaccine. *ACS Nano* 2021;**15**:15754−70.
54. Li M, Huang YX, Wu JC, Li SP, Mei M, Chen HX, et al. A PEG-lipid-free COVID-19 mRNA vaccine triggers robust immune responses in mice. *Mater Horiz* 2023;**10**:466−72.
55. Tan CW, Chia WN, Qin X, Liu P, Chen MI, Tiu C, et al. A SARS-CoV-2 surrogate virus neutralization test based on antibody-mediated blockage of ACE2-spike protein−protein interaction. *Nat Biotechnol* 2020;**38**:1073−8.
56. Li D, Martinez DR, Schafer A, Chen H, Barr M, Sutherland LL, et al. Breadth of SARS-CoV-2 neutralization and protection induced by a nanoparticle vaccine. *Nat Commun* 2022;**13**:6309.
57. Xiao TS, Lu JM, Zhang J, Johnson RI, McKay LGA, Storm N, et al. A trimeric human angiotensin-converting enzyme 2 as an anti-SARS-CoV-2 agent. *Nat Struct Mol Biol* 2021;**28**:202−9.